Article

Optical cooling by interfacial charge transfer in 2D heterostructures

https://doi.org/10.1038/s41586-026-10662-w

Received: 2 April 2025

Accepted: 14 May 2026

Published online: 24 June 2026

Check for updates

Jiamin Lin[1,13], Baixu Xiang[2,3,13], Renguang Liu[4,13], Jinyang Ling[1,13], Gang Wang[5], Le Zhang[1], Li Li[1], Hua Li[1], Dongxu Zhang[1], Zhexing Duan[6], Qi Zhang[6], Changjin Wan[7], Wei Wang[8], Xingzhi Wang[9], Junhao Lin[5,10], Huajian Gao[4]✉, Qihua Xiong[2,3,11,12]✉ & Weigao Xu[1]✉

Optical refrigeration, or laser cooling of solids[1], offers a cryogen-free route to temperature control for quantum and electronic systems. Existing progress[2–8] relies on a phonon-assisted up-conversion photoluminescence approach, which remains constrained by stringent material and excitation requirements. Here we demonstrate a distinct route, interfacial-charge-transfer-driven optical cooling, in two-dimensional semiconductor heterostructures. Photo-excited carriers in WSe_2 cross a type-II junction into $MoSe_2$ or WS_2, extracting lattice energy nonradiatively—through a phonon-assisted interfacial charge transfer process. Raman and photoluminescence measurements show prominent low-temperature signatures in the WSe_2 layer, with transient absorption spectroscopy identifying a phonon-assisted, barrier-activated interlayer charge transfer. Molecular dynamics simulations show a prominent interfacial thermal resistance sustaining the temperature gradient. This barrier-mediated phonon extraction bypasses the need for near-unity quantum efficiency or resonant excitation, offering a promising strategy for cryogen-free refrigeration and thermal management in quantum, optoelectronic and nanoscale systems.

Proposed by Pringsheim in 1929 (ref. 1) and first demonstrated in rare-earth doped solids[2], solid-state laser cooling relies on phonon-assisted up-conversion photoluminescence (UCPL), in which photons carry away lattice heat by annihilating phonons. Despite decades of progress[3–10], solid-state laser cooling remains limited by its stringent requirements: near-unity quantum efficiency, minimal parasitic absorption and precisely tuned excitation energy. These conditions are difficult to meet in most semiconductors and severely restrict material choices and device integration[11].

Two-dimensional (2D) semiconductors provide a new arena for manipulating light–matter and heat–matter interactions. Their atomic thickness enables the assembly of van der Waals heterostructures with precisely engineered interfacial components[12], twist angles[13,14] and interlayer distances[15]. With all atoms exposed at surfaces and interfaces, the electronic, optical and phononic behaviours are governed by interlayer interactions. Although monolayer transition metal dichalcogenides exhibit strong electron–phonon coupling and UCPL has been demonstrated in these materials[16,17], laser cooling has yet to be realized because their photoluminescence quantum yield (PLQY) remains far below the cooling threshold[18]. Although ongoing efforts seek to further improve quantum efficiency[19], alternative strategies beyond UCPL are highly desirable to explore the feasibility of laser cooling in 2D materials. Although potential cooling mechanisms have been theoretically explored[20,21], experimental validation remains unknown.

Inspired by recent advances in interfacial engineering, particularly the manipulation of carrier motions in 2D semiconductors[15,22], we propose an alternative cooling mechanism, termed interfacial-charge-transfer-driven (ICT-driven) optical refrigeration. The fundamental prerequisite for refrigeration in semiconductors is the effective extraction of phonons. Previous studies have established the presence of momentum mismatching[23,24] and phonon participation[25–27] in the interfacial charge-transfer processes of 2D heterobilayers, motivating us to explore whether this phonon-assisted charge transfer could facilitate optical refrigeration. An energy barrier is required in this process to enable the dissipation of phonon energy—namely, heat. However, in the extensively studied strongly coupled heterobilayers, previous theoretical predictions and ultrafast measurements suggest that the charge transfer proceeds without an energy barrier[23,26,28]. This realization leads to our first challenge: to tune the interfacial coupling and introduce an energy barrier that allows for unidirectional phonon extraction during interlayer charge transfer.

Another challenge lies in achieving lattice thermal isolation of the cooled material from the environmental heat sink, in which manipulating out-of-plane thermal transport through interlayer coupling

[1]State Key Laboratory of Analytical Chemistry for Life Science, Key Laboratory of Mesoscopic Chemistry of MOE, School of Chemistry, Nanjing University, Nanjing, China. [2]State Key Laboratory of Low-Dimensional Quantum Physics, Department of Physics, Tsinghua University, Beijing, China. [3]Beijing Academy of Quantum Information Sciences, Beijing, China. [4]Mechano-X Institute, Applied Mechanics Laboratory, Department of Engineering Mechanics, Tsinghua University, Beijing, China. [5]State Key Laboratory of Quantum Functional Materials, Department of Physics, and Guangdong Basic Research Center of Excellence for Quantum Science, Southern University of Science and Technology (SUSTech), Shenzhen, China. [6]Key Laboratory of Quantum Materials and Devices of Ministry of Education, School of Physics, Southeast University, Nanjing, China. [7]National Laboratory of Solid-State Microstructures, School of Electronic Science and Engineering and Collaborative Innovation Center of Advanced Microstructures, Nanjing University, Nanjing, China. [8]State Key Laboratory of Analytical Chemistry for Life Science, Chemistry and Biomedicine Innovation Center (ChemBIC), School of Chemistry, Nanjing University, Nanjing, China. [9]Department of Physics, Xiamen University, Xiamen, China. [10]Quantum Science Center of Guangdong-Hong Kong-Macao Greater Bay Area (Guangdong), Shenzhen, China. [11]Frontier Science Center for Quantum Information, Beijing, China. [12]Collaborative Innovation Center of Quantum Matter, Beijing, China. [13]These authors contributed equally: Jiamin Lin, Baixu Xiang, Renguang Liu, Jinyang Ling. ✉e-mail: gao.huajian@tsinghua.edu.cn; qihua_xiong@tsinghua.edu.cn; xuwg@nju.edu.cn

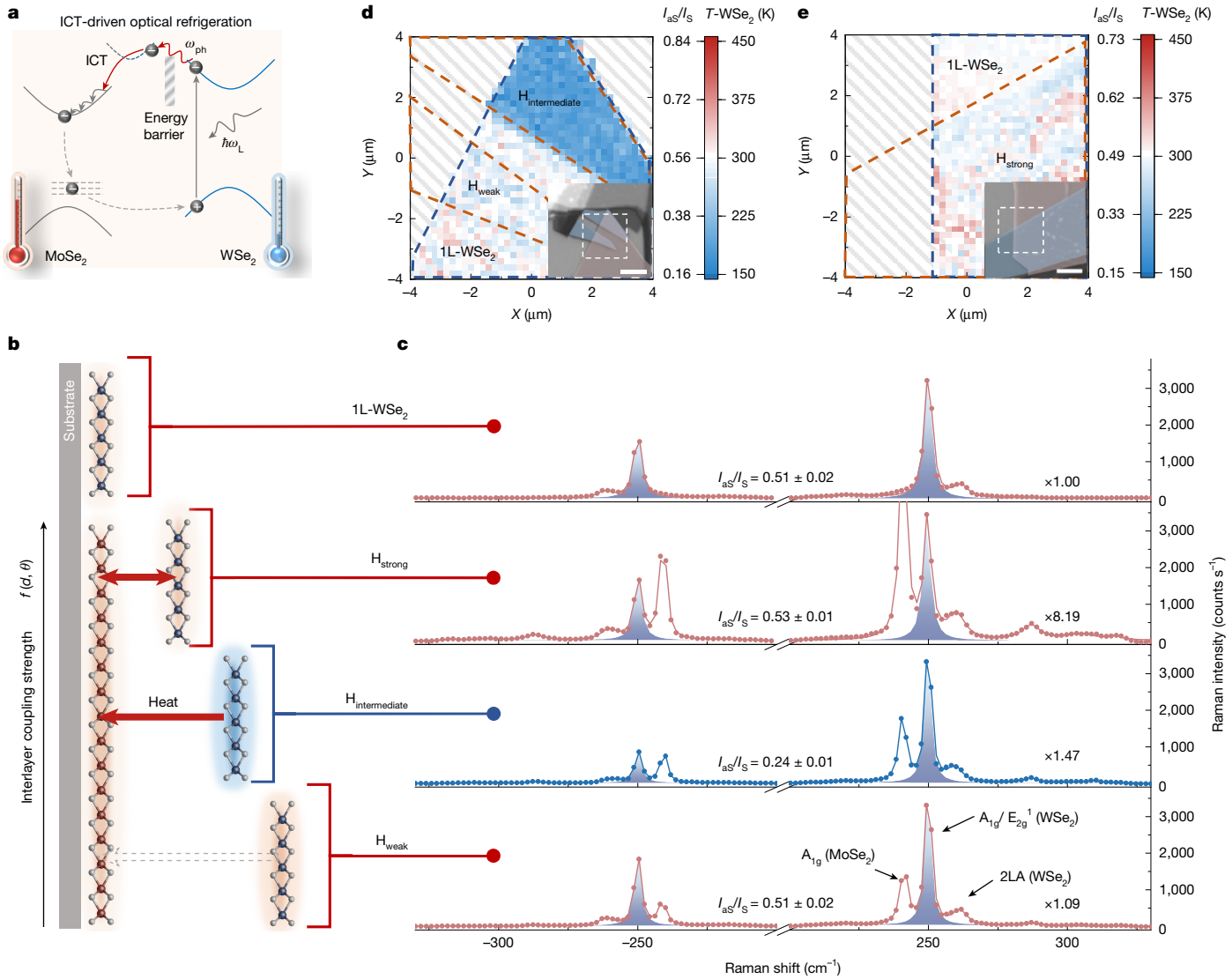

Fig. 1 | The concept of ICT-driven optical refrigeration and observation of anomalous phonon population of WSe_2 in a WSe_2/$MoSe_2$–$H_{intermediate}$ heterobilayer. a, The concept of phonon-assisted interfacial charge-transfer in type-II 2D semiconductor heterostructures. The phonon consumption and unidirectional heat transfer lead to cooling of the electron donor layer. **b**, Schematic of heterostructure with different interlayer coupling strengths, which is a function of interlayer distance (d) and twist angle (θ). **c**, Raman spectra of the 1L-WSe_2, H_{weak}, $H_{intermediate}$ and H_{strong}. The blue fillings mark the $A_{1g}/E_{2g}{}^1$ mode of WSe_2 (about 249 cm^{-1}). All spectra are normalized according to the Stokes intensity. The uncertainties in the I_{aS}/I_S values are derived from the Raman peak fitting process, as described in the Methods, 'Raman thermometry'. **d**, Temperature image of H_{weak} and $H_{intermediate}$, according to the Raman mapping at ±249 cm^{-1} ($A_{1g}/E_{2g}{}^1$ mode of WSe_2). The WSe_2 component in $H_{intermediate}$ exhibits a spatial temperature standard deviation of about 18 K. The inset shows the optical image of WSe_2/$MoSe_2$ heterobilayer with H_{weak} and $H_{intermediate}$ regions. **e**, Temperature image of H_{strong}, according to the Raman mapping at ±249 cm^{-1} ($A_{1g}/E_{2g}{}^1$ mode of WSe_2). The corresponding T-WSe_2 scales on the colour bar are derived from I_{aS}/I_S using the γ-corrected Raman thermometry calibration described later. The inset shows the optical image of WSe_2/$MoSe_2$ heterobilayer with H_{strong} region. A 532 nm (2.33 eV) laser with a power of approximately 200 μW was used for excitation (**c**–**e**). The regions enclosed by the blue and orange dashed lines mark the WSe_2 and $MoSe_2$ monolayer regions and the grey shadows mark the area without WSe_2. Scale bar, 5 μm (**d**,**e**).

engineering may be beneficial[29,30]. Unlike UCPL, in which heat escapes by emission, here the heat is transferred to another material layer through interlayer charge transfer. This creates steep temperature gradients across sub-nm separations, necessitating high interfacial thermal resistance to suppress heat backflow. The rational design and control of interfacial interactions are, therefore, essential for tackling both challenges.

The concept of ICT-driven optical refrigeration is schematically shown in Fig. 1a. Taking a WSe_2/$MoSe_2$ heterobilayer as an example: (1) on excitation, hot electrons in the conduction band of the WSe_2 layer tend to transfer to the conduction band of the $MoSe_2$ layer, while an interfacial energy barrier must be overcome and phonon participation is required; (2) dominant thermal relaxation processes occur within the $MoSe_2$ layer, and the heat can subsequently be transferred to the external heat sink; (3) an interfacial thermal resistance between WSe_2 and $MoSe_2$ suppresses heat reflux back into the cooled WSe_2 layer, enabling the practical realization of a net cooling effect. Following this proposed model, our first key task is to construct an energy barrier for interfacial charge transfer by tuning the interlayer coupling state.

Anomalous phonon population

We first constructed WSe_2/$MoSe_2$ heterostructures with different interlayer coupling strengths. Emerging studies have recently indicated the possibility of using interlayer coupling as a knob for the design and tailoring of 2D heterostructures[15,31,32]. Here, we will continue to adopt

a previously established spacer-free approach[12,15,33]. Heterobilayers were prepared by dry transfer with careful adjustment of interlayer distance d and twist angle θ. A typical weakly coupled sample (H_{weak}) retains monolayer-like optical signatures with minimal PL quenching and maintains an overall large interlayer spacing (>2 nm), which is expected to be reliably prepared by avoiding any thermal treatment. A typical strongly coupled sample (H_{strong}) has an interlayer distance close to the intrinsic van der Waals spacing of about 0.6 nm (ref. 34) and a twist angle of about 0° (or 60°), ensuring a strong interlayer hybridization of electron wavefunctions[12]. In H_{strong}, efficient interlayer charge transfer leads to substantial quenching of intralayer exciton emission, accompanied by the emergence of interlayer exciton emission[12]. However, neither H_{weak} nor H_{strong} shall be an ideal candidate for potential optical refrigeration. For H_{weak}, weak interlayer coupling leads to low charge-transfer efficiency[15], resulting in insufficient phonon extraction for refrigeration. For the H_{strong} sample, the absence of an adequate interfacial energy barrier prevents phonon consumption in the target component, and its large lattice thermal conductivity facilitates phonon backflow, likely diminishing the interfacial temperature difference. An intermediate coupling regime then becomes a central focus, which may simultaneously fulfil the two essential requirements for optical cooling: efficient phonon extraction and suppressed thermal backflow. With mild thermal treatment and large twist angles (details in the Methods), specimens with intermediate coupling states between H_{weak} and H_{strong} exhibit moderate PL intensity, about 1% of that in H_{weak}, but still about one order of magnitude higher than in H_{strong} (Supplementary Fig. 1). No interlayer exciton emission is detected in the intermediate region at room temperature. The out-of-plane A_{1g} Raman intensities also decrease progressively from H_{weak}, intermediate region, to H_{strong}. We found it is necessary to use the term '$H_{intermediate}$' to define intermediate samples that fulfil the above requirements and exhibit distinct thermal properties as compared with H_{weak} and H_{strong}. Figure 1b shows H_{weak}, $H_{intermediate}$ and H_{strong} with monotonously increasing interlayer coupling strength. More details about this classification are presented in Supplementary Note 1, Supplementary Fig. 2 and Supplementary Table 1.

Before investigating the cooling effect of these samples, a reliable thermometry method is required. As the primary form of heat, the frequency and population of phonons directly reflect the lattice temperature, probed using Raman-active phonon modes. Here we extract lattice temperatures from phonon populations using the anti-Stokes/Stokes Raman intensity ratio (I_{aS}/I_S) (refs. 35,36). This phonon-based thermometry offers layer-specific vibrational 'fingerprints' across only van der Waals separation, providing highly localized temperature information. Intrinsic and environmentally robust temperature information can be extracted, as this temperature sensing mechanism is inherently resistant to both interlayer hybridization and charge transfer. A notable limitation is that, as will be discussed later, caution is required regarding the resonance effect[35].

Figure 1c shows the anti-Stokes and Stokes Raman spectra of WSe_2 monolayer and $WSe_2/MoSe_2$ heterobilayers of H_{weak}, $H_{intermediate}$ and H_{strong} with a 532 nm (2.33 eV) laser at ambient conditions. The setup is shown in Supplementary Fig. 3a. Filter response correction was applied to the acquired Raman spectra (Supplementary Fig. 4). Representative Raman peaks at around ±240 cm^{-1}, ±249 cm^{-1} and ±261 cm^{-1} correspond to A_{1g} of $MoSe_2$, $A_{1g}/E_{2g}{}^1$ of WSe_2 (degenerate A_{1g} and $E_{2g}{}^1$ phonons) and 2LA of WSe_2, respectively[37,38]. Fitted with single Lorentzian (blue shadow), the I_{aS}/I_S intensity ratios of the $A_{1g}/E_{2g}{}^1$ (WSe_2) mode in the monolayer, H_{weak} and H_{strong} are close, which are 0.51 ± 0.02, 0.53 ± 0.01 and 0.51 ± 0.02, respectively. The I_{aS}/I_S of $A_{1g}/E_{2g}{}^1$ (WSe_2) in $H_{intermediate}$ is greatly decreased, with a value of only 0.24 ± 0.01. As a reference, the I_{aS}/I_S ratios of A_{1g} for the $MoSe_2$ component (±240 cm^{-1}) for monolayer, H_{weak}, $H_{intermediate}$ and H_{strong} are calculated to be 0.44 ± 0.04, 0.43 ± 0.01, 0.42 ± 0.01 and 0.45 ± 0.02, respectively (Supplementary Fig. 5a). Other vibrational modes in $H_{intermediate}$-WSe_2 also exhibit such anomalous I_{aS}/I_S reduction (Supplementary Table 2 and Supplementary Note 2.1), probably indicating a lowered phonon population and a temperature reduction. This ratio drop is not confined to individual spots but across the entire $H_{intermediate}$ region, whereas the WSe_2 component in H_{strong} or H_{weak} gives an overall I_{aS}/I_S close to the monolayers (Fig. 1d,e).

Although the results are encouraging, it is necessary to verify whether the anomalous I_{aS}/I_S ratio observed in $H_{intermediate}$ is from optical refrigeration, rather than a resonance effect[35,39]. In sideband Raman cooling reports, a decreased I_{aS}/I_S ratio can emerge under precisely controlled blue-detuned excitation of the B-exciton in 3L-WS_2 because of asymmetric resonance enhancement[39]. Here, however, room-temperature transmission spectra confirm that our excitation energy (2.33 eV) falls at the red-detuned sideband of the A′ exciton (2.46 eV) of 1L-WSe_2 which is rather distant, and that excitonic absorption remains relatively flat at excitation energy independent of coupling (Supplementary Fig. 6). This uniformity precludes pronounced resonance-enhancement discrepancies between different coupling states. The substantial I_{aS}/I_S drop only in $H_{intermediate}$ securely reflects genuine depletion of the phonon population rather than a simple resonance effect (details in Supplementary Note 2.2).

To correlate the I_{aS}/I_S intensity ratio to the temperature, a calibration is required. According to the Bose–Einstein distribution, the phonon population for k^{th} mode $\bar{n}_{MX_2-k}$ (M = W, Mo and X = Se) is given by $\bar{n}_{MX_2-k}=\left[\exp\left(\frac{\hbar\omega_{MX_2-k}}{k_B T_{MX_2}}\right)-1\right]^{-1}$, where $\hbar$ is the reduced Planck's constant, k_B is Boltzmann's constant. The ratio of anti-Stokes to Stokes intensity for k^{th} mode ρ_{MX_2-k} can be directly related with phonon population through the following relationship $\rho_{MX_2-k}=\frac{I_{aS}}{I_S}=\gamma\left(\frac{\omega_0+\omega_{MX_2-k}}{\omega_0-\omega_{MX_2-k}}\right)^4\frac{\bar{n}_{MX_2-k}}{\bar{n}_{MX_2-k}+1}$, where I_{aS} and I_S are the anti-Stokes and Stokes intensity of k^{th} vibrational mode with frequency ω_{MX_2-k}, ω_0 is the frequency of excitation laser, and γ is a phenomenological correction factor that encapsulates both instrument response characteristics and resonance effects (Supplementary Note 2). γ can be experimentally determined by substituting the experimental I_{aS}/I_S into the equation when the material temperature is the same as the set environment temperature T_{env}.

We then performed Raman measurements on the samples in their various coupling states at varying environment temperature (T_{env}) (Fig. 2a–c). For the non-cooling monolayers, γ can be readily extracted as the material is in thermal equilibrium with the environment. For $H_{intermediate}$-WSe_2, however, as the probe laser itself induces a cooling effect, a 'cooling-free' baseline for calibration is not yet experimentally feasible. Despite that $H_{intermediate}$-WSe_2 shows a distinct trend from the others, the other non-cooling $MoSe_2$ and WSe_2 components in heterostructures share similar I_{aS}/I_S–T_{env} curves with their monolayer counterpart, respectively, whatever states they are in. Combined with the flat absorption profiles near excitation wavelength across all coupling states (Supplementary Fig. 6), an adjacent monolayer may serve well as a proxy for calibration of heterostructures assuming that the resonance difference among states is negligible as discussed before, so that the temperature drop in $H_{intermediate}$ can also be deduced. As shown in Fig. 2d, by multiplying the room temperature γ of monolayer WSe_2 to the original curve following Bose–Einstein distribution, a calibration curve is acquired. This γ-corrected curve matches well with the I_{aS}/I_S data near room temperature and serves as the primary calibration method used throughout this paper. More details about calibration are discussed in Supplementary Note 2, Supplementary Fig. 7 and Supplementary Table 3.

The lattice temperature can then be calculated from the I_{aS}/I_S ratios in Fig. 1c–e, with $H_{intermediate}$-WSe_2 being about 187 K, lower than that of monolayer WSe_2 (300 K), WSe_2 in H_{weak} (about 307 K), and WSe_2 in H_{strong} (around 318 K). For the $MoSe_2$ component, I_{aS}/I_S ratios for H_{weak}, $H_{intermediate}$ and H_{strong} give lattice temperatures of about 291 K, 297 K and 317 K, respectively.

In laser cooling of solid-state matter, up-conversion fluorescence characteristics are commonly used as temperature indicators[2,4,5]. Typically, a PL blue shift and a narrowing of the full width at half maximum (FWHM) are observed during cooling, primarily due to lattice contraction[4]. Conversely, heterobilayer formation induces a PL red-shift

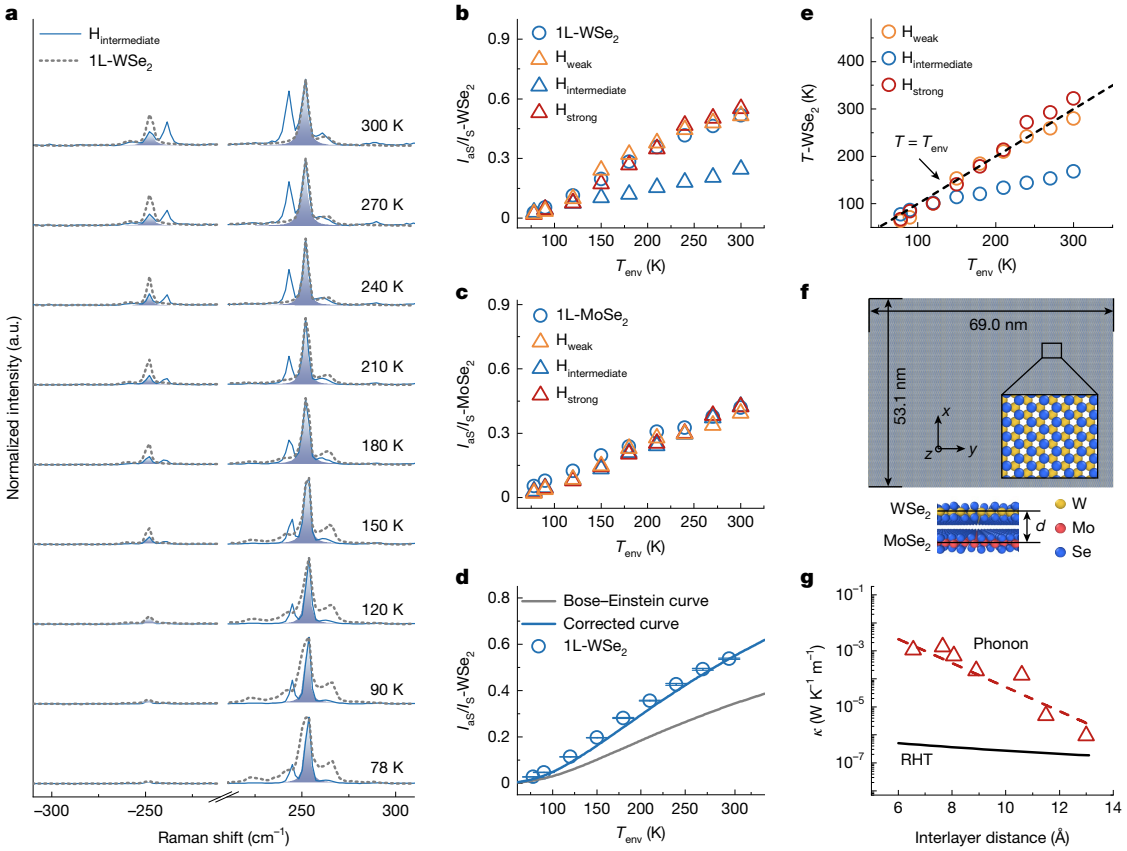

Fig. 2 | Raman thermometry and environment-dependent cooling behaviour. a, Raman spectra of 1L-WSe_2 (grey dotted lines) and $H_{intermediate}$ (blue lines) taken from 77 K to 300 K under 532 nm excitation at 10 μW to prevent possible heating effects. The blue fillings mark the $A_{1g}/E_{2g}{}^1$ mode of WSe_2 in $H_{intermediate}$. All Raman intensities were normalized to the $A_{1g}/E_{2g}{}^1$ mode of WSe_2 and vertically offset for visualization. **b**,**c**, I_{as}/I_S of WSe_2 (**b**) and $MoSe_2$ (**c**) in H_{weak}, $H_{intermediate}$, H_{strong} and monolayers as a function of environment temperature (T_{env}). **d**, The calibration for 1L-WSe_2 with a room-temperature γ. The grey and blue lines are the uncorrected curve following the Bose–Einstein distribution and the γ-corrected calibration curve, respectively. The error bars represent the uncertainties introduced during the Raman peak fitting process, as described in the Methods, 'Raman thermometry'. **e**, Temperature of WSe_2 in H_{weak}, $H_{intermediate}$ and H_{strong} as a function of environment temperature. The dashed black line is the temperature of T_{env}. **f**, Atomic configuration of the 2H-stacked $WSe_2/MoSe_2$ heterobilayer used in molecular dynamics simulation. The bottom panel provides a side view, illustrating the bilayer stacking sequence along the z-axis with an interlayer distance (d). **g**, Relationship between interlayer distance (in Å) and the thermal conductivity (in W K^{-1} m^{-1}) of $WSe_2/MoSe_2$ heterobilayers, with the y-axis presented on a logarithmic scale. RHT, radiative heat transfer; a.u., arbitrary units.

and a broadened FWHM, caused by layer hybridization and interlayer charge transfer[40]. Despite this, the fluorescence of the A-exciton in $H_{intermediate}$-WSe_2 exhibits a pronounced blue shift compared with H_{strong}, approaching the peak position in pristine 1L-WSe_2 or even surpassing monolayers in some $H_{intermediate}$ specimens (Supplementary Fig. 8). A narrowing of FWHM is also observed in $H_{intermediate}$. These prominent low-temperature signatures collectively support the optical refrigeration of WSe_2 component in $H_{intermediate}$ heterobilayers. More details are provided in Supplementary Note 3 and Supplementary Fig. 9.

The impact of the interlayer twist angle θ is investigated as another key parameter of the interlayer coupling strength (Supplementary Fig. 10). A total of 21 $WSe_2/MoSe_2$ heterobilayer samples were fabricated, covering a twist angle range from 0° to 60°. To minimize the influence of interlayer spacing variations, all samples in this experiment were annealed at 200 °C for 1 h under an Ar/H_2 atmosphere to ensure a close van der Waals contact. We found that when the twist angle is near 20° or 40°, the cooling behaviour is well-preserved even after high-temperature annealing. As the large twist angle induces substantial k-space mismatch, this behaviour may be attributed to the phonon involvement during interfacial charge transfer to conserve momentum. Details of the factors influencing the coupling states and the properties of different states are discussed in Supplementary Note 1. Apart from $WSe_2/MoSe_2$, ICT-driven optical refrigeration was also observed in intermediately coupled WSe_2/WS_2 samples with a similar type-II band alignment, where Raman thermometry indicated net cooling of the WSe_2 component by about 117 K (Supplementary Fig. 11).

T_{env}-dependent unidirectional heat flux

The necessity of phonon participation to overcome the interlayer energy barrier indicates that ICT-driven cooling is a highly temperature-dependent process. Temperature-dependent optical refrigeration experiments were conducted from 78 K to 300 K. To evaluate the temperature of the WSe_2 component in $H_{intermediate}$ at lower T_{env}, another calibration fitting was applied (Supplementary Note 2.4). The calculated lattice temperatures (T-WSe_2) of WSe_2 in heterobilayers and the set environment temperatures (T_{env}) are plotted in Fig. 2e. The temperature of WSe_2 in H_{weak} and H_{strong}, and SiO_2/Si substrate (shown in Supplementary Fig. 7b) were in good agreement with T_{env}. For $H_{intermediate}$-WSe_2, an even lower lattice temperature can be achieved when T_{env} decreases. However, the cooling magnitude (ΔT) also progressively decreases, eventually becoming indistinguishable from the non-cooling reference samples when $T_{env} \leq 120$ K (Fig. 2e). This is consistent with a reduced phonon population and less efficient phonon-assisted charge transfer under low-temperature conditions. The phonon population $\bar{n}$ of the $A_{1g}/E_{2g}{}^1$ mode decreases from 0.435 at

300 K to 0.053 at 120 K, accompanied by an increase in the corresponding ground-state occupancy probability $P_{\bar{n}=0} = 1/(1+\bar{n})$ from 69.7% to 94.9%. These statistics indicate that ICT-driven optical cooling will be difficult when most lattice phonons are at their zero-point energy.

Under ambient conditions, the >100 K temperature difference between the WSe_2 and $MoSe_2$ across a nanometre-scale gap implies a substantial thermal gradient (about 10^{11} K m^{-1}). This raises a fundamental question about the mechanisms sustaining this substantial temperature difference in heterobilayers. To address this, we performed molecular dynamics simulations of phonon-mediated cross-plane heat transport in $WSe_2/MoSe_2$ heterobilayers, to assess whether interlayer thermal transport can be sufficiently suppressed within the adopted interaction model. Motivated by previous studies of van der Waals heterostructures, we further examined the dependence of interlayer thermal transport on spacing[41,42].

We varied the interlayer spacing from 0.66 nm (close to the van der Waals equilibrium spacing) to 1.30 nm. Representative equilibrium configurations are shown in Fig. 2f. Using non-equilibrium molecular dynamics (NEMD) simulations, we calculated the interlayer thermal transport under an imposed thermal bias. As shown in Fig. 2g and Supplementary Fig. 12a–g, the effective interlayer thermal conductivity decays exponentially from 1.08×10^{-3} W K^{-1} m^{-1} to 9.29×10^{-7} W K^{-1} m^{-1} with increasing interlayer spacing, spanning more than three orders of magnitude. This pronounced decay indicates that modest changes in the van der Waals gap can strongly suppress phonon backflow and provide a plausible mechanism for sustaining the observed temperature contrast. We further evaluated near-field thermal radiation and found its contribution to be negligible in this spacing range (Fig. 2g, black line, and Supplementary Note 4.1).

Recognizing that thermal transport across the material–substrate interface also plays a crucial part, we also calculated the interfacial thermal conductance between $MoSe_2$ and SiO_2/Si substrate. The calculated thermal conductance of 15.47 ± 7.11 MW m^{-2} K^{-1} (Supplementary Fig. 12h) exceeds that of the $WSe_2/MoSe_2$ heterobilayer by about one order of magnitude even at 0.66 nm spacing (1.65 ± 0.04 MW m^{-2} K^{-1}), which highlights the role of substrate in facilitating heat dissipation from the heterobilayer system to the environment. Experimentally, for samples in good contact with the substrate, the bottom $MoSe_2$ layers show little measurable heating in $H_{intermediate}$. By contrast, weak substrate coupling leads to a higher $MoSe_2$ temperature (Supplementary Fig. 5b,c). Conversely, when the stacking order is reversed and the bottom WSe_2 is brought into good thermal contact with the substrate, the cooling signature is suppressed (Supplementary Fig. 5d). Similar cooling behaviour is not limited to $H_{intermediate}$ samples on SiO_2/Si substrates, but was consistently observed also on sapphire and diamond substrates, as shown in Supplementary Fig. 5d.

Ultrafast dynamics of phonon-assisted ICT

Previous studies suggested the absence of an energy barrier during interlayer charge transfer in strongly coupled heterobilayers through either an adiabatic or a phonon-emission process[26,28]. However, this barrier is indispensable for ICT-driven cooling. To clarify the actual contribution of phonons in interfacial charge transfer events, temperature-dependent ultrafast interlayer charge-transfer dynamics are highly demanded. Here, the WSe_2/WS_2 combination was selected to investigate the ICT behaviour in $H_{intermediate}$ and H_{strong} at different temperatures, as the narrower bandgap of the electron donor (WSe_2) enables its selective excitation in this combination, allowing us to readily track the charge transfer time[43,44] (Supplementary Fig. 13a). We have used an obliquely incident pump beam (Supplementary Fig. 3b) at about 740 nm (approximately 1.68 eV) to excite the electrons in the WSe_2 counterpart and a broadband probe beam ranging from 450 nm (2.76 eV) to 820 nm (1.51 eV) to monitor the dynamics of the electron excitation in WSe_2 and the interlayer charge transfer to WS_2 layer.

Figure 3a shows a 2D plot of transient absorption spectra of $H_{intermediate}$ at an initial stage of the dynamical process (−0.18 ps to 0.43 ps) at 298 K. As indicated in Fig. 3a (vertical white lines), after a delay time (τ) of approximately 56 fs, the ground-state bleaching (GSB) feature of the A-exciton of WS_2 (red horizontal dashed line) appears. The delay time exactly corresponds to the previously reported electron-transfer time scale from the conduction band of WSe_2 to WS_2[44]. Notably, as shown in Fig. 3b,c, the delay time increases to approximately 85 fs at 78 K and 114 fs at 10 K. The τ increases with decreasing T, indicating the existence of an energy barrier in the ICT process in $H_{intermediate}$[45]. Following the Arrhenius equation $\ln k_T = -\frac{E_a}{k_B} \times \frac{1}{T} + \ln A$ (where k_T is the measured ICT rate at temperature T, and $k_T = 1/\tau$; A is the frequency factor; and k_B is the Boltzmann constant), an estimated effective ICT energy barrier E_a of 0.3 meV for 10–77 K and 3.8 meV for 77–298 K is shown by temperature-dependent τ values (Fig. 3d, blue solid dots). In $WSe_2/MoSe_2$ heterobilayer samples, the ICT energy barrier is estimated to be about 33.75 meV at 298 K (Supplementary Note 5.1 and Supplementary Fig. 14). It is worth mentioning that, although the laser introduces much excess energy with respect to the WSe_2 band edge, the deduced energy barrier is relatively small. Our data indicate that this behaviour is governed by momentum conservation requirements, and the 'energy barrier' reflects the necessity of phonon involvement. This is consistent with our angle-dependent experiments. For WSe_2/WS_2–H_{weak}, the barely observable GSB feature in WS_2 suggests that there is negligible interlayer charge transfer (Supplementary Fig. 13b). For WSe_2/WS_2–H_{strong}, a robust (thus temperature-independent) ICT time of approximately 47 fs was observed for 298 K, 78 K and 10 K, as shown in Fig. 3d (blue hollow dots) and Supplementary Fig. 13c–e, which is consistent with previous studies[28]. This temperature-dependent ICT behaviour in $H_{intermediate}$ samples validates the participation of phonons in the electron transfer process. To achieve net cooling, the charge transfer efficiency should be near unity with an ultrafast rate, avoiding intralayer hot carrier relaxation. In the $H_{intermediate}$ state, the ultrafast ICT process preempts the intralayer relaxation, with an efficiency approaching 99.7%, demonstrating that hot carriers are effectively extracted across the interface before dissipating their excess energy as phonons (Supplementary Note 5.2 and Supplementary Fig. 15), while the approximately 0.3% residual inevitably leaves minor heat in the layer. Suppressing this residual hot-carrier relaxation within the charge donor layer is essential for achieving an even lower cooling temperature in the future.

After the ICT process, to complete the cooling cycle, the transferred excited-state electrons must ultimately return to the WSe_2 layer. Their recombination dynamics can be tracked by the bleaching decay of A-excitons of WS_2 and WSe_2. The prolonged decay times of both WS_2 and WSe_2 in $H_{intermediate}$ (blue curves) compared with those in H_{strong} (orange curves), as shown in Fig. 3e,f, indicate a suppressed direct interlayer recombination pathway that can be attributed to the weaker coupling of $H_{intermediate}$ than H_{strong}. As Fig. 3g shows, the recombination dynamics are independent of excitation density, further excluding the Auger process[23]. The excited-state electrons are then left in the WS_2 component for a longer time to go through other routes. Increasing recombination time with decreasing temperature (Fig. 3h) indicates dominant indirect transition paths[46]. We assume that defects or trap states may mediate the recombination in the WS_2 layer. The transferred excited-state electrons gradually step down to lower energy states and leave heat in the WS_2 layer before they go back to the valence band of WSe_2. For the $WSe_2/MoSe_2$ heterobilayers, the cooling cycle is similar, as WSe_2 has the highest conduction and valence band energy, and the charge transfer direction is conserved.

Excitation and material tolerance

In UCPL-based laser cooling of solids, the excitation energy of the incident laser is restricted to be slightly red-detuned, corresponding to a limited 'cooling zone'[3]. Moreover, despite the high sensitivity to

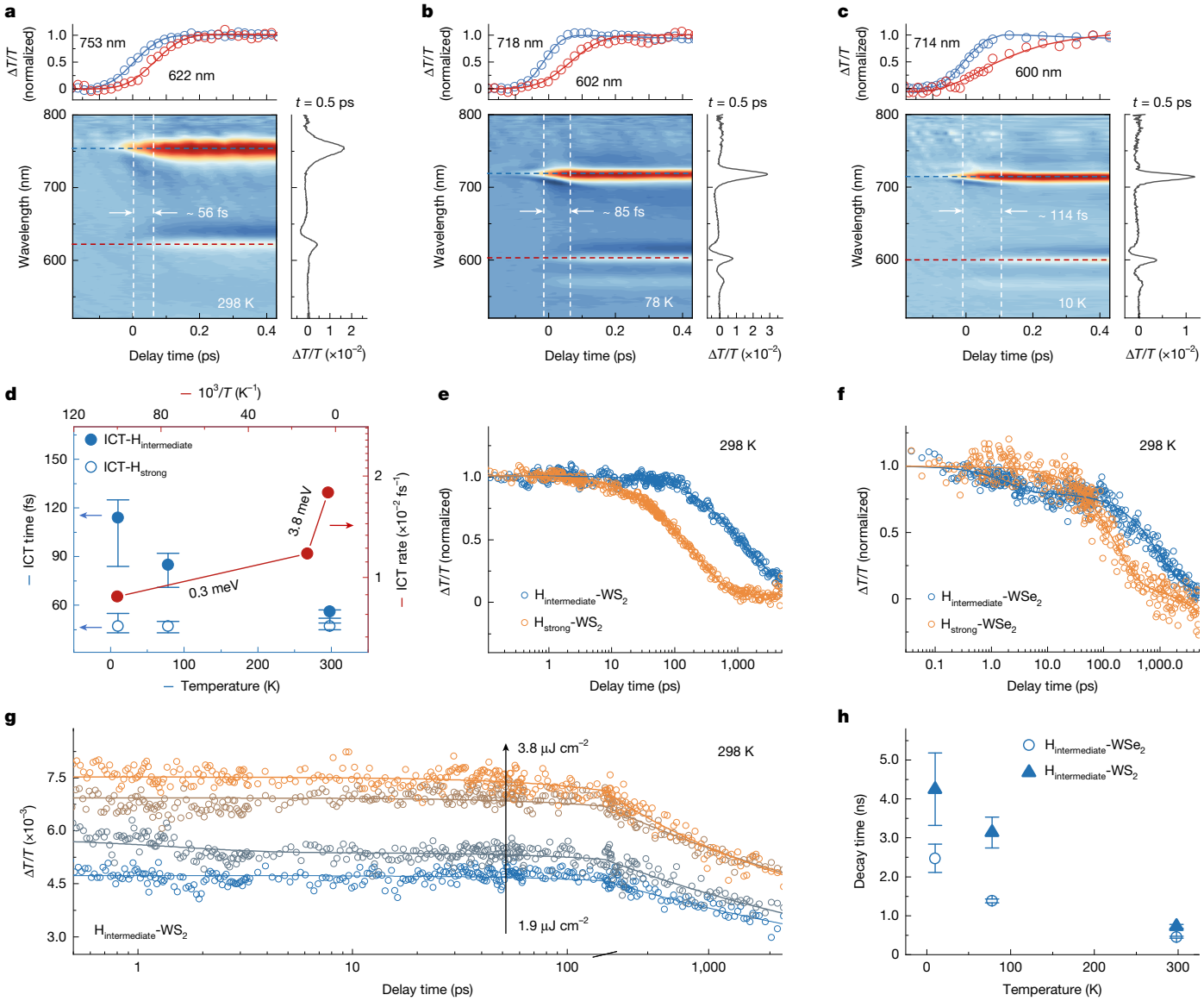

Fig. 3 | Phonon-mediated charge separation and recombination behaviour in heterobilayers with different interlayer coupling strengths. a–**c**, Transient absorption measurements of WSe_2/WS_2–$H_{intermediate}$ at 298 K (**a**), 78 K (**b**) and 10 K (**c**). In the main panels, the differential transmission ($\Delta T/T(\lambda, t)$) of the broadband probe beam is shown in 2D false-colour maps plotted against the pump–probe delay time and the wavelength. In all cases, the spectra of the excitation pulse (710–750 nm) are adjusted to overlap with the absorption of WSe_2. The top panels show the normalized signal dynamics evaluated at fixed wavelengths, indicated on the colour maps by horizontal colour-coded dashed lines. The right panels show dynamic spectral signatures of the signal evaluated at fixed delay times *t*. The white vertical dashed lines mark the midpoint of the rising-edge for ICT time calculation. **d**, The ICT time (blue axes) of $H_{intermediate}$ (solid blue dots), H_{strong} (open blue dots) and ICT rate (red axes) in $H_{intermediate}$ (solid red dots) as a function of temperature. The error bars were estimated by picking the rising-edge threshold time as 40% and 60% of the signal amplitude in **a**–**c**. **e**,**f**, Charge recombination kinetics of WS_2 (**e**) and WSe_2 (**f**) layers in $H_{intermediate}$ (blue lines) and H_{strong} (orange lines) at room temperature. **g**, Electron population kinetics in WS_2 layer for $H_{intermediate}$ at different excitation densities (from bottom to top: 1.9 μJ cm^{-2}, 2.5 μJ cm^{-2}, 3.2 μJ cm^{-2} and 3.8 μJ cm^{-2}). **h**, The fitted decay time of the $H_{intermediate}$-WSe_2 and $H_{intermediate}$-WS_2 as a function of temperature. The error bars represent the standard errors of the fitted decay time.

excitation conditions, efforts to prepare cooling-grade materials with maximized PLQY and minimized parasitic absorption have remained the primary obstacle for realizing optical cooling in solids. By contrast, the scheme of ICT-driven optical refrigeration alleviates these constraints.

We used a dual-beam optical setup (Fig. 4a, inset) to monitor the cooling behaviour in $H_{intermediate}$ under varied excitation conditions, with an attempt to test the excitation tolerance of ICT-driven optical cooling. A 532 nm laser served as the main cooling beam (5 μW), whereas a tunable white light laser with an adjustable output wavelength ranging from 650 nm (1.91 eV) to 800 nm (1.55 eV) was used as another beam to perturb the cooling effect. As shown in Fig. 4a, the temperature of $H_{intermediate}$-WSe_2 under all perturbing beam excitations remains consistently below room temperature, even with a power up to 100 μW. Noticeably, the temperature under the perturbing beams with 703 nm (1.76 eV) and 743 nm (1.67 eV) showed a slight increase. We speculate that a resonance effect with the B-exciton of $MoSe_2$ and A-exciton of WSe_2 is responsible for this variation.

Power dependence of the refrigerating effect is shown in Fig. 4b, ranging from 5 nW to 500 μW. The 1L-WSe_2 exhibits relatively stable I_{as}/I_S values in the range of 0.52 ± 0.02 for the whole excitation power range (corresponding to *T*-WSe_2 = 298 ± 10 K, red circles), with an unnoticeable optical heating effect. For the $H_{intermediate}$ region, WSe_2 shows a relatively stable temperature of around 200 K under 1–500 μW

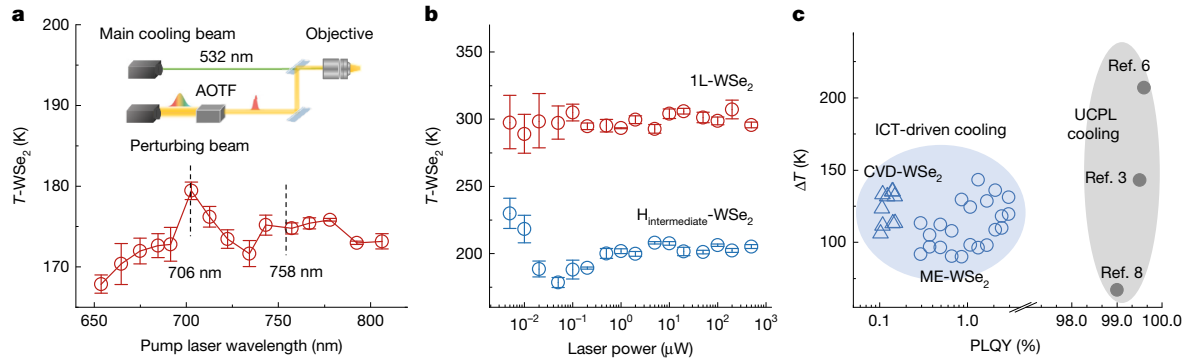

Fig. 4 | Excitation and material tolerance of ICT optical refrigeration. **a**, Temperature of the WSe_2 component in $H_{intermediate}$ as a function of pump laser wavelength. The inset shows a schematic of the dual-beam setup featuring a 532 nm probe laser and a supercontinuum laser source, coupled with a monochromator for selecting the desired excitation wavelength as the pump laser for perturbation. AOTF, acousto-optic tunable filter. **b**, Temperature of 1L-WSe_2 and $H_{intermediate}$-WSe_2 as a function of laser power. The calibration factor in **b** was taken from 1L-WSe_2 under 5 nW excitation. **c**, The cooling temperature (ΔT) of WSe_2 in $H_{intermediate}$ with mechanical-exfoliation WSe_2 (ME-H, hollow circle) and chemical vapour deposition-grown WSe_2 (CVD-H, triangle) measured at varied PLQY values. For UCPL-based cooling in Yb^{3+}-doped systems (solid grey dots; data adapted from refs. 3,6,8), the PLQY is subject to a stringent requirement of being near unity. Error bars in **a** and **b** represent the uncertainties derived from Raman-thermometry fitting, as described in Methods, 'Raman thermometry'.

excitation. Lowering the power leads to a minimum lattice temperature reaching about 178 K at 50 nW. Below this power, the temperature began to recover towards ambient, reaching approximately 230 K at 5 nW. Although some $H_{intermediate}$ samples do not exhibit a temperature dip, the temperature recovery at extremely low power and the stabilization above 1 μW are broadly observed. The lattice temperature is assumed to be dictated by several competing factors: the phonon-assisted interlayer charge transfer that consumes phonons, and the residual carrier relaxation at the donor layer or interfacial heat backflow that creates phonons. When increasing the excitation power, the laser-driven cooling and heating effects become dominant, reaching a stable balance to create the observed cooling saturation near 200 K. The rather low saturation point of power may be due to the extremely small thermal load of the WSe_2 layer.

A near-unity PLQY[11] is essential for minimizing potential heating in the UCPL cooling process. The difference here for ICT-driven cooling process is that the requirement for high quantum efficiency may be bypassed. The PLQY values of the as-exfoliated WSe_2 samples were measured to be in the range of 0.3–3%. Even for chemical vapour deposition (CVD)-grown WSe_2 with lower PLQY (about 0.1%), the cooling effect persists (Fig. 4c).

Discussion

In this work, we propose an ICT-driven strategy for optical refrigeration. Conceptually, as a viable complement to Pringsheim's picture, the ICT-driven process extends optical cooling to nonradiative pathways, enabling phonon extraction through engineered interfacial carrier motions. The scheme tolerates low quantum yield and relaxed excitation conditions, providing a general framework for directing energy flow at the atomic scale. Our experimental observations collectively point to net cooling in type-II semiconductor heterostructures and provide evidence for phonon participation during interlayer charge transfer. Several directions merit further investigation, including more accurate micro- and nanoscale thermometry, a deeper understanding of the phonon-assisted ICT pathways and extension to broader materials systems. Related interfacial carrier-transfer concepts have been explored theoretically[20,21], but by distinct mechanisms, such as exploiting upward band offsets in type-I heterostructures for evaporative carrier cooling. These interfacial charge transfer strategies hold great potential for cryogen-free refrigeration and thermal management in quantum and nanoscale systems. More broadly, this approach enables access to low-temperature electronic[47], excitonic[14,22,48,49] and phononic[50] phenomena under ambient or elevated temperatures.

Online content

Any methods, additional references, Nature Portfolio reporting summaries, source data, extended data, supplementary information, acknowledgements, peer review information; details of author contributions and competing interests; and statements of data and code availability are available at https://doi.org/10.1038/s41586-026-10662-w.

1. Pringsheim, P. Zwei Bemerkungen über den Unterschied von Lumineszenz- und Temperaturstrahlung. *Z. Physik* **57**, 739–746 (1929).
2. Epstein, R. I., Buchwald, M. I., Edwards, B. C., Gosnell, T. R. & Mungan, C. E. Observation of laser-induced fluorescent cooling of a solid. *Nature* **377**, 500–503 (1995).
3. Seletskiy, D. V. et al. Laser cooling of solids to cryogenic temperatures. *Nat. Photon.* **4**, 161–164 (2010).
4. Zhang, J., Li, D., Chen, R. & Xiong, Q. Laser cooling of a semiconductor by 40 kelvin. *Nature* **493**, 504–508 (2013).
5. Ha, S.-T., Shen, C., Zhang, J. & Xiong, Q. Laser cooling of organic-inorganic lead halide perovskites. *Nat. Photon.* **10**, 115–121 (2016).
6. Melgaard, S. D., Albrecht, A. R., Hehlen, M. P. & Sheik-Bahae, M. Solid-state optical refrigeration to sub-100 Kelvin regime. *Sci. Rep.* **6**, 20380 (2016).
7. Mobini, E. et al. Laser cooling of ytterbium-doped silica glass. *Commun. Phys.* **3**, 134 (2020).
8. Topper, B. et al. Laser cooling ytterbium doped silica by 67 K from ambient temperature. *Opt. Express* **32**, 3660–3672 (2024).
9. Roder, P. B., Smith, B. E., Zhou, X., Crane, M. J. & Pauzauskie, P. J. Laser refrigeration of hydrothermal nanocrystals in physiological media. *Proc. Natl Acad. Sci. USA* **112**, 15024–15029 (2015).
10. Zhang, Q. et al. Phonon-assisted anti-Stokes lasing in ZnTe nanoribbons. *Adv. Mater.* **28**, 276–283 (2015).
11. Zhang, Z. et al. Principles for demonstrating condensed phase optical refrigeration. *Nat. Rev. Phys.* **7**, 149–153 (2025).
12. Rivera, P. et al. Valley-polarized exciton dynamics in a 2D semiconductor heterostructure. *Science* **351**, 688–691 (2016).
13. Cao, Y. et al. Unconventional superconductivity in magic-angle graphene superlattices. *Nature* **556**, 43–50 (2018).
14. Tran, K. et al. Evidence for moiré excitons in van der Waals heterostructures. *Nature* **567**, 71–75 (2019).
15. Xu, W. G. et al. Correlated fluorescence blinking in two-dimensional semiconductor heterostructures. *Nature* **541**, 62–67 (2017).
16. Xu, W., Zhao, Y., Shen, C., Zhang, J. & Xiong, Q. Phonon-assisted upconversion photoluminescence in monolayer $MoSe_2$ and WSe_2. *Acta Chim. Sin.* **73**, 959–964 (2015).
17. Jones, A. M. et al. Excitonic luminescence upconversion in a two-dimensional semiconductor. *Nat. Phys.* **12**, 323–327 (2016).
18. Wang, S. et al. Light-emitting diodes based on intercalated transition metal dichalcogenides with suppressed efficiency roll-off at high generation rates. *Nat. Electron.* **8**, 56–65 (2025).
19. Lien, D.-H. et al. Electrical suppression of all nonradiative recombination pathways in monolayer semiconductors. *Science* **364**, 468–471 (2019).
20. Dalla Valle, P., Bescond, M., Michelini, F. & Cavassilas, N. Laser cooling in semiconductor heterojunctions by extraction of photogenerated carriers. *Phys. Rev. Appl.* **20**, 014066 (2023).

21. Dalla Valle, P., Bescond, M., Michelini, F. & Cavassilas, N. Solar refrigeration based on impact ionization in a transition metal dichalcogenides superlattice. *J. Phys. Chem. C* **128**, 4905–4913 (2024).
22. Sun, Q. et al. Designable excitonic effects in van der Waals artificial crystals with exponentially growing thickness. *Nat. Commun.* **16**, 2712 (2025).
23. Zhu, H. et al. Interfacial charge transfer circumventing momentum mismatch at two-dimensional van der Waals heterojunctions. *Nano Lett.* **17**, 3591–3598 (2017).
24. Schmitt, D. et al. Formation of moiré interlayer excitons in space and time. *Nature* **608**, 499–503 (2022).
25. Long, R. & Prezhdo, O. V. Quantum coherence facilitates efficient charge separation at a MoS_2/$MoSe_2$ van der Waals junction. *Nano Lett.* **16**, 1996–2003 (2016).
26. Wang, Y., Wang, Z., Yao, W., Liu, G.-B & Yu, H. Interlayer coupling in commensurate and incommensurate bilayer structures of transition-metal dichalcogenides. *Phys. Rev. B* **95**, 115429 (2017).
27. Zheng, Q. et al. Phonon-assisted ultrafast charge transfer at van der Waals heterostructure interface. *Nano Lett.* **17**, 6435–6442 (2017).
28. Zhou, H., Zhao, Y. & Zhu, H. Dielectric environment-robust ultrafast charge transfer between two atomic layers. *J. Phys. Chem. Lett.* **10**, 150–155 (2018).
29. Kim, S. E. et al. Extremely anisotropic van der Waals thermal conductors. *Nature* **597**, 660–665 (2021).
30. Zhang, R. et al. Extreme thermal insulation and tradeoff of thermal transport mechanisms between graphene and WS_2 monolayers. *Adv. Mater.* **36**, 2313753 (2024).
31. Xia, J. et al. Strong coupling and pressure engineering in WSe_2-$MoSe_2$ heterobilayers. *Nat. Phys.* **17**, 92–98 (2020).
32. Alexeev, E. M. et al. Resonantly hybridized excitons in moiré superlattices in van der Waals heterostructures. *Nature* **567**, 81–86 (2019).
33. Li, H. et al. Spontaneous polarity flipping in a 2D heterobilayer induced by fluctuating interfacial carrier flows. *Nano Lett.* **21**, 6773–6780 (2021).
34. Dickinson, R. G. & Pauling, L. The crystal structure of molybdenite. *J. Am. Chem. Soc.* **45**, 1466–1471 (1923).
35. Zhang, J., Zhang, Q., Wang, X., Kwek, L. C. & Xiong, Q. Resolved-sideband Raman cooling of an optical phonon in semiconductor materials. *Nat. Photon.* **10**, 600–605 (2016).
36. Meng, Q. et al. Local heating and Raman thermometry in a single molecule. *Sci. Adv.* **10**, eadl1015 (2024).
37. Zhao, Y. et al. Interlayer breathing and shear modes in few-trilayer MoS_2 and WSe_2. *Nano Lett.* **13**, 1007–1015 (2013).
38. Lu, X., Luo, X., Zhang, J., Quek, S. Y. & Xiong, Q. Lattice vibrations and Raman scattering in two-dimensional layered materials beyond graphene. *Nano Res.* **9**, 3559–3597 (2016).
39. Lai, J. M., Sun, Y. J., Tan, Q. H., Tan, P. H. & Zhang, J. Laser cooling of a lattice vibration in van der Waals semiconductor. *Nano Lett.* **22**, 7129–7135 (2022).
40. Sigger, F. et al. Spectroscopic imaging ellipsometry of two-dimensional TMDC heterostructures. *Appl. Phys. Lett.* **121**, 071102 (2022).
41. Ding, Z., Pei, Q. X., Jiang, J. W., Huang, W. & Zhang, Y. W. Interfacial thermal conductance in graphene/MoS_2 heterostructures. *Carbon* **96**, 888–896 (2016).
42. Sood, A. et al. Engineering thermal transport across layered graphene-MoS_2 superlattices. *ACS Nano* **15**, 19503–19512 (2021).
43. Ceballos, F., Bellus, M. Z., Chiu, H.-Y. & Zhao, H. Ultrafast charge separation and indirect exciton formation in a MoS_2-$MoSe_2$ van der Waals heterostructure. *ACS Nano* **8**, 12717–12724 (2014).
44. Hong, X. et al. Ultrafast charge transfer in atomically thin MoS_2/WS_2 heterostructures. *Nat. Nanotechnol.* **9**, 682–686 (2014).
45. Atkins, P., Paula, J. D. & Keeler, *J. Atkins' Physical Chemistry* (Oxford Univ. Press, 2018).
46. Choi, J. et al. Twist angle-dependent interlayer exciton lifetimes in van der Waals heterostructures. *Phys. Rev. Lett.* **126**, 047401 (2021).
47. Ghiotto, A. et al. Quantum criticality in twisted transition metal dichalcogenides. *Nature* **597**, 345–349 (2021).
48. Yu, L. et al. Observation of quadrupolar and dipolar excitons in a semiconductor heterotrilayer. *Nat. Mater.* **22**, 1485–1491 (2023).
49. Wu, Z. et al. Realization of two-dimensional spin-orbit coupling for Bose-Einstein condensates. *Science* **354**, 83–88 (2016).
50. Quan, J. et al. Phonon renormalization in reconstructed MoS_2 moiré superlattices. *Nat. Mater.* **20**, 1100–1105 (2021).

Methods

Preparation of heterobilayers

Transition metal dichalcogenide (TMDC) monolayers (1L-WSe_2, 1L-$MoSe_2$ and 1L-WS_2) were obtained by mechanical exfoliation from bulk crystals (HQ Graphene) using Ultra-Tape. Here, 1L refers to a TMDC monolayer consisting of three atomic planes (X–M–X). The layer number of each constituent monolayer was identified from its characteristic PL emission before heterostructure assembly. The bottom layers ($MoSe_2$ or WS_2) were then dry-transferred onto the substrate, followed by annealing at 100 °C for 10 min, unless otherwise noted. The heterobilayers were further assembled using the aligned dry transfer method with the assistance of polydimethylsiloxane (PDMS). Most of our samples were transferred onto SiO_2/Si substrates with an oxide layer of 80 nm thick, if not otherwise noted. The samples for transient and steady-state absorption measurements were fabricated on the transparent sapphire substrates to enable transmission-mode measurements. The coupling states of the heterobilayers were controlled by twist angle and post-processing conditions. H_{weak} samples with a large interlayer distance were prepared without any heating. The strongly coupled heterobilayers, termed H_{strong}, were prepared by annealing at 200 °C in an Ar/H_2 atmosphere for 1 h, and with a twist angle close to 0° or 60°. Heterobilayers exhibiting an optical cooling effect, with an interlayer coupling strength between H_{weak} and H_{strong} (termed $H_{intermediate}$), were prepared by heating at 75 °C for 15 min, unless otherwise noted, with a preferred twist angle between 20° and 40°. The twist angles were first roughly estimated based on the alignment of the straight edges of the two monolayer flakes during stacking, and then confirmed with polarization-resolved second-harmonic generation method using a 780 nm (1.59 eV) pulsed laser (NPI Laser, Rainbow, 80 MHz, <80-fs pulse duration). These are the recommended procedures intended to yield the corresponding coupling state with the highest possible likelihood. In the fabrication of CVD heterobilayers (CVD-H), 1L-WSe_2 grown by CVD was sourced from Zhongke Crystal Materials (Dongguan).

Raman thermometry

All Raman spectra were acquired using 532 nm excitation (unless otherwise noted) under a single grating window, on a confocal Raman spectrometer (Horiba LabRAM HR Evolution) equipped with 600- and 1,800-lines-per-mm gratings. The schematic optical measurement setup is provided in Supplementary Fig. 3a. A 100× objective lens (numerical aperture (NA) = 0.9, Olympus) was used to focus the laser normally onto the sample, forming a spot with a radius of about 0.7 μm, and to collect the backscattered signal. Multiple BragGrate notch filters (BNFs) were used to cut off the Rayleigh scattering background under 532 nm continuous-wave laser excitation (CNI Laser MSL-FN-532). The response differences of BNFs (optical density = 3, FWHM of about 5–10 cm^{-1}) between anti-Stokes and Stokes signals were corrected by continuous white light. A transmission efficiency curve is used to calibrate the intensity of signals to correct the effect of BNFs in the spectroscopy system before each measurement. A halogen lamp was used as a light source, and two reflection spectra before and after adding BNFs were given in Supplementary Fig. 4. We subtracted the baseline from the raw spectra and did Lorentzian peak fitting of signals. The fitting error of I_{aS}/I_S is calculated according to $\sigma_\rho = \sqrt{\left(\frac{\sigma_{I_{aS}}}{I_S}\right)^2 + \left(\frac{I_{aS} \times \sigma_{I_S}}{{I_S}^2}\right)^2}$, which is used for the calculation of the temperature error introduced during the Raman fitting process. Here, $\sigma_{I_{aS}}$ and σ_{I_S} are the standard deviations of anti-Stokes and Stokes signals, which were calculated by the difference between the integrated area intensities of the experimental data and the fitted spectra. The anti-Stokes and Stokes Raman spectral mappings were carried out using a galvo-scanning system with a step size of 0.1–0.3 μm. More details on Raman thermometry can be found in Supplementary Note 2.

Fluorescence microscopy and spectroscopy

Wide-field fluorescence images of the samples were acquired by a fluorescence microscope equipped with a high-speed S-CMOS camera (Teledyne Photometrics Prime 95B). The samples were excited using an Olympus U-HGLGPS lamp through a 530/40 nm band-pass filter, and the emitted light was filtered by a 570 nm long-pass dichroic mirror. PL spectra were measured on the same Horiba HR Evolution spectrometer with a 100-lines-per-mm grating. In this work, PL measurements were excited with a 2.33 eV continuous-wave laser. Their excitation power is specifically mentioned for each experiment. A supercontinuum laser source with an acousto-optic tunable filter (AOTF) was used to select excitation wavelength, which served as the pump beam to investigate the effect of excitation wavelength on ICT-driven optical cooling. All ambient temperature and atmospheric pressure tests were collected by a 100× objective lens (NA = 0.9, Olympus). In situ temperature-dependent experiments were performed in a continuous-flow liquid-nitrogen cryostat (Cryo Industries of American). A 100× correction collar objective lens (NA = 0.85, Leica) was used to collect the signal to avoid refraction interference introduced by the window glass. We used Labspec6 software for data processing. All acquired signals are calibrated with neon standard signals and are not smoothed.

Transient absorption spectroscopy

The pump–probe transient absorption experiments were performed on a custom-built free-space optical setup integrated with a commercial transient transmission spectrometer (Helios Fire, Ultrafast Systems). Femtosecond pulses at 800 nm (at a repetition rate of 1 kHz and a pulse duration of about 35 fs) were provided by a Ti:sapphire amplifier (Coherent) and split into two beams. One was sent into an optical parametric amplifier to generate pump pulses with tunable photon energies, and the other was focused into the sapphire crystal to generate broadband white light (450–820 nm) for probe pulses, controlled by a motorized delay stage. The pump and probe beams were focused and overlapped on the sample surface in a non-collinear configuration, with 200 μm and 6 μm spot sizes in diameter, respectively. The transmitted probe beam was detected by a spectrometer equipped with a back-thinned charge-coupled detector (CCD) linear detector. The schematic pump–probe optical setup is provided in the Supplementary Fig. 3b. By scanning the grating and delay stage, we were able to measure the pump-induced absorption change as a function of energy and delay time. Moreover, the pump pulse was compressed by chirped mirrors, which resulted in an instrumental response function (IRF) to be approximately 40 fs. In our ultrafast experiments, the pump fluence was kept below 6 μJ cm^{-2} (the injected carrier density of about 10^{11} cm^{-2}), keeping the sample signals in the linear response regime. All transient absorption spectra were subsequently chirp-corrected to ensure accurate temporal alignment across probe wavelengths before data fitting. The transient kinetics were analysed using a bi-exponential decay function ($I = A_1 e^{-\frac{t}{\tau_r}} + A_2 e^{-\frac{t}{\tau_{nr}}}$), where the faster decay time constant (τ_r) and the slower decay time constant (τ_{nr}) correspond to radiative lifetime and non-radiative lifetime, respectively, A_1 and A_2 are the amplitude coefficients.

Computational details

All molecular dynamics simulations were performed using the large-scale atomic/molecular massively parallel simulator (LAMMPS)[51]. Details of the interatomic potentials and interaction parameters are provided in Supplementary Note 4.2. The validation of these potential functions is presented in Supplementary Note 4.3 and Supplementary Fig. 16. The net gap distance in the intermediate $MoSe_2$/WSe_2 state in this work is much smaller than the mean free path of air molecules, resulting in substantial suppression of air conductivity due to the Knudsen effect[52]. Meanwhile, we also calculated the near-field thermal radiation between the heterostructure layers, which was found to be on the order of 10^{-8} to 10^{-7}. Therefore, the phonon contribution to thermal transport

was mainly considered in the simulations. The parameters used in the near-field radiative heat transfer calculation are summarized in Supplementary Table 4. Owing to the relatively large interlayer spacings investigated in this study, which exceed those typically used in previous molecular dynamics simulations[41,42], artificial constraints were applied to maintain structural stability at these distances, as described in Supplementary Note 4.2.

Before thermal transport simulations, the atomic configurations were optimized by structural relaxation using the conjugate gradient method to achieve energy minimization. The system was then equilibrated under an isothermal–isobaric ensemble (NPT ensemble, constant number of particles, pressure and temperature) for 50 ps, with zero lateral stress applied in the *x*- and *y*-directions using a Nosé–Hoover barostat. Following pressure equilibration, the $MoSe_2$ and WSe_2 layers were independently thermalized under a canonical ensemble (NVT) for 100 ps at their respective target temperatures of 350 K and 250 K using a Nosé–Hoover thermostat. All simulations used a time step of 0.5 fs to integrate the equations of motion.

Following the methodology in ref. 53, we incorporated the nonlinear component of the temperature profile and computed the temperature difference, rather than the temperature gradient, to more accurately characterize cross-layer thermal transport in our NEMD simulations. After equilibrating the system in a microcanonical ensemble, we applied the 'fix ehex' command to add and remove energy at equal rates in the $MoSe_2$ and WSe_2 layers, respectively. Details of the thermal conductivity calculation method are provided in Supplementary Note 4.4. NEMD simulations of $MoSe_2$ in contact with a SiO_2 substrate were conducted under similar conditions, with full details in Supplementary Note 4.5. Because the measured temperature differences are sensitive to the imposed energy exchange rates, careful selection of these values was essential. Excessively high- or low-energy flux could lead to prolonged relaxation times. Preliminary tests were performed to estimate the thermal conductivity κ for each case, followed by formal simulations. Each simulation was run for at least 10 ns to ensure that a steady state was reached, characterized by a stable temperature difference between the two layers. Complete coupling coefficients and representative thermalization trajectories are summarized in Supplementary Tables 5 and 6 and Supplementary Fig. 12h.

Methodology for PLQY measurement

The PLQY measurement platform was constructed using a 532 nm continuous-wave laser (CNI Laser MDL-III-532) as the excitation source. The collimated laser beam was focused onto the sample through a 50× objective lens (Olympus LMPlanFL, NA = 0.5). Emitted photons were collected by the same objective in a backscattering geometry and directed to a Horiba HR550 spectrometer coupled with a thermoelectrically cooled CCD detector (Horiba SynapsePlus BIVS, 1,024 × 256 pixels). The incident laser power was calibrated using a photodiode power meter (ThorLabs PM100D + S130VC) and modulated using neutral density filters to maintain excitation intensities below 200 μW to avoid sample damage.

The spectral wavelength accuracy of the spectrometer was verified using a calibration lamp (Ocean Optics HG-1), with the 546.08 nm emission line as the reference. The IRF was characterized by irradiating the system with a broadband tungsten halogen lamp (Ocean Optics HL-2000-LL) stabilized at 2,800 K, simulating a Lambertian blackbody source. The IRF correction factor $\eta(\lambda)$, accounting for wavelength-dependent detection efficiency, was calculated as: $\eta(\lambda) = \frac{I_{\mathrm{measured}}(\lambda)}{I_{\mathrm{reference}}(\lambda)}$, where $I_{\mathrm{measured}}(\lambda)$ is the irradiance signal of the lamp measured through the optical path and $I_{\mathrm{reference}}(\lambda)$ represents the pristine spectral irradiance of the lamp.

The absolute PLQY was calculated using the relation $\mathrm{QY} = \frac{I_{WSe_2} \times R_{\mathrm{Lbr}} \times \eta_{\mathrm{system}(532)}}{I_{\mathrm{Lbr}} \times A_{WSe_2} \times \eta_{\mathrm{system}(\lambda)}}$, where I_{WSe_2} and I_{Lbr} are integrated intensities of the collected PL spectra of WSe_2 and diffuse reflection spectrum of a 532 nm continuous-wave laser focused on a Lambertian reflector, respectively. R_{Lbr} is the reflectivity of the Lambertian reflector (about 99%). A_{WSe_2} is the optical absorption of WSe_2 at 532 nm, and $A_{WSe_2} = 1 - R - T$, where R denotes the reflection and T denotes the transmission. $\eta_{\mathrm{system}}(\lambda)$ is the response efficiency of the optical system to the light at wavelength λ (IRF-corrected).

The PLQY of monolayer WSe_2 (mechanically exfoliated and CVD-grown) was measured under varying excitation powers, followed by lattice temperature measurements of the WSe_2 component in $H_{\mathrm{intermediate}}$ heterostructures under the same conditions. The results are presented in Fig. 4c.

Cross-sectional structural analysis

Cross-sectional transmission electron microscopy specimens were prepared using a ThermoFisher Helios NanoLab 600i focused ion beam system. Before focused ion beam milling, a protective layer approximately 50 nm in thickness was formed by spin-coating a carbon-based ink solution onto the sample/substrate surface. Subsequently, a 1–1.5 μm thick tungsten–carbon (W–C) protective layer was deposited over the carbon layer to mitigate ion-beam-induced damage during milling. Cross-sectional lamellae approximately 50 nm in thickness were fabricated using a standard lift-out procedure. Final thinning and removal of surface amorphization were achieved by sequential Ga^+ ion beam polishing at progressively reduced acceleration voltages of 5 kV and 2 kV.

Atomically resolved high-angle annular dark-field scanning transmission electron microscopy imaging was performed using a probe-corrected JEOL ARM-200F transmission electron microscope operated at an accelerating voltage of 200 kV. A collection angle range of 68–200 mrad and a convergence semi-angle of 29.2 mrad were used. The beam current was maintained below 30 pA for all experiments to minimize electron beam damage.

The coordinates of the top and bottom interfacial profiles across a region of approximately 100 nm were extracted using the CalAtom software package[54]. Statistical analysis of the interlayer distances was subsequently performed based on the extracted coordinate data.

Data availability

The datasets generated during and/or analysed during this study are available from the corresponding authors on request. Source data are provided with this paper.

Code availability

The custom Python code used to reconstruct the far-infrared dielectric functions, perform the $WSe_2/MoSe_2$ near-field radiative heat transfer calculations and evaluate model sensitivity is available at Zenodo[55] (https://doi.org/10.5281/zenodo.19697929). The actively maintained development repository is available at GitHub (https://github.com/RenguangLiu/NFRHT-MoSe2toWSe2).

51. Thompson, A. P. et al. LAMMPS - a flexible simulation tool for particle-based materials modeling at the atomic, meso, and continuum scales. *Comput. Phys. Commun.* **271**, 108171 (2022).
52. Devienne, F. M. *Advances in Heat Transfer* Vol. 2, 271–356 (Academic Press, 1965).
53. Li, Z. et al. Influence of thermostatting on nonequilibrium molecular dynamics simulations of heat conduction in solids. *J. Chem. Phys.* **151**, 234105 (2019).
54. Zhang, Q., Zhang, L. Y., Jin, C. H., Wang, Y. M. & Lin, F. CalAtom: a software for quantitatively analysing atomic columns in a transmission electron microscope image. *Ultramicroscopy* **202**, 114–120 (2019).
55. Liu, R. RenguangLiu/NFRHT-MoSe2toWSe2: Code for NFRHT calculation in MoSe2/WSe2 heterobilayers. *Zenodo* https://doi.org/10.5281/zenodo.19697780 (2026).

Acknowledgements We thank L. Yang for discussions on near-field radiative heat transfer.

Author contributions W.X. and Jiamin Lin conceived the initial idea. W.X., Q.X. and Jiamin Lin designed the experiments. Jiamin Lin fabricated the samples and performed the spectroscopy measurement experiments with help from L.Z., Jinyang Ling, L.L. and D.Z.; B.X. and Q.X. optimized the temporal resolution and conducted the pump–probe transient absorption measurements. R.L. and H.G. conducted the molecular dynamics simulations. Z.D. and Q.Z.

contributed to the PLQY measurements. G.W. and Junhao Lin performed the STEM-related experiments. Jiamin Lin, B.X., R.L., and Jinyang Ling analysed the data with discussions from H.L., X.W., W.W., C.W., H.G., Q.X. and W.X.; Jiamin Lin organized all experimental data. Jiamin Lin, B.X., R.L., Jinyang Ling, H.G., Q.X. and W.X. wrote the paper with input from all authors.

Funding W.X. and Q.X. acknowledge support from the National Key R&D Program of China (2022YFA1204700). W.X. acknowledges support from the National Natural Science Foundation of China (22333004, 223B2304, 22203042 and 22173044). This work has been supported in part by the New Cornerstone Science Foundation (Q.X.). This work was supported by the Mechano-X Institute of Tsinghua University (H.G.). G.W. and Junhao Lin acknowledge support from the National Key Basic Research and Development Program of China (2024YFA1408102 and 2024YFA1409100), the National Natural Science Foundation of China (52473302, 12404017, 12461160252 and T2525009), Guangdong Basic Science Foundation (2023B1515120039), Natural Science Foundation of Guangdong Province, China (2025A1515011998), and Quantum Science Strategic Special Project from the Quantum Science Center of Guangdong–Hong Kong–Macao Greater Bay Area (GDZX2301006 and SZZX2301004). X.W. acknowledges the support of the National Key R&D Program of China (2022YFA1602704), the National Natural Science Foundation of China (62275225), and the 111 Project (B16029).

Competing interests The authors declare no competing interests.

Additional information

Supplementary information The online version contains supplementary material available at https://doi.org/10.1038/s41586-026-10662-w.

Correspondence and requests for materials should be addressed to Huajian Gao, Qihua Xiong or Weigao Xu.

Peer review information *Nature* thanks the anonymous reviewers for their contribution to the peer review of this work. Peer reviewer reports are available.